Supporting Information

High Resolution XFEL Structure of the Soluble Methane Monooxygenase Hydroxylase Complex with its Regulatory Component at Ambient Temperature in Two Oxidation States

Vivek Srinivas,[†,#] Rahul Banerjee,[‡,#] Hugo Lebrette,[†] Jason C. Jones,[‡] Oskar Aurelius,[†] In-Sik Kim,[§] Cindy C. Pham,[§] Sheraz Gul,[§] Kyle D. Sutherlin,[§] Asmit Bhowmick,[§] Juliane John,[†] Esra Bozkurt,[†] Thomas Fransson,[&] Pierre Aller,[+,¤] Agata Butryn,[+,¤] Isabel Bogacz,[§] Philipp Simon,[§] Stephen Keable,[§] Alexander Britz,[¶] Kensuke Tono,[~] Kyung Sook Kim,[^] Sang-Youn Park,[^] Sang Jae Lee,[^] Jaehyun Park,[^] Roberto Alonso-Mori,[¶] Franklin D. Fuller,[¶] Alexander Batyuk,[¶] Aaron S. Brewster,[§] Uwe Bergmann,[•] Nicholas K. Sauter,[§] Allen M. Orville,[+,¤] Vittal K. Yachandra,[§] Junko Yano,[*,§] John D. Lipscomb,[*,‡] Jan Kern,[*,§] and Martin Högbom[*,†]

[†]Department of Biochemistry and Biophysics, Stockholm University, Arrhenius Laboratories for Natural Sciences, Stockholm, Sweden.

[‡]Department of Biochemistry, Molecular Biology and Biophysics, University of Minnesota, Minneapolis, Minnesota 55391 U.S.A.

[§]Molecular Biophysics and Integrated Bioimaging Division, Lawrence Berkeley National Laboratory, Berkeley, California 94720 U.S.A.

[¶]LCLS, SLAC National Accelerator Laboratory, Menlo Park, California 94025 U.S.A.

[+]Diamond Light Source, Harwell Science and Innovation Campus, Didcot, Oxfordshire, OX11 0DE, UK

[¤]Research Complex at Harwell, Rutherford Appleton Laboratory, Didcot, Oxfordshire, OX11 0FA, UK

[&]Interdisciplinary Center for Scientific Computing, University of Heidelberg, 69120 Heidelberg, Germany.

[~]Japan Synchrotron Radiation Research Institute, Sayo-gun 679 5198, Japan

[^]Pohang Accelerator Laboratory, Gyeongsangbuk-do 37673, South Korea

[•]Stanford PULSE Institute, SLAC National Accelerator Laboratory, Menlo Park, California, 94025 U.S.A.

Joint First Authors

[#]V.S. and R.B. contributed equally to the creation of this study.

Supporting Information Table of Contents

SUPPLEMENTAL RESULTS

Table S1. X-ray Data Collection and Refinement Statistics for MMOH:MMOB Complex in the Diferric, Diferrous, Reoxidized States, and the t = 0 Diferrous State Before O_2 Exposure.

Dataset (PDB Code)	Diferric MMOH:MMOB (PDB 6YD0)	Diferrous MMOH:MMOB (PDB 6YDI)	Reoxidized MMOH:MMOB (PDB 6YDU)	t = 0 Diferrous MMOH:MMOB (PDB 6YY3)
Wavelength	1.30644	1.30448	1.30396	1.318066
XFEL source	LCLS MFX	LCLS MFX	LCLS MFX	PAL-XFEL NCI
Spacegroup	$P4_12_12$	$P4_12_12$	$P4_12_12$	$P4_12_12$
Cell dimensions (Å)	106.9, 106.9, 303.9	106.9, 106.9, 303.9	106.9, 106.9, 304.1	106.0, 106.0, 301.0
Cell angles (deg)	90, 90, 90	90, 90, 90	90, 90, 90	90, 90, 90
Resolution range[a] (Å)	33.00-1.95 (2.02-1.95)	33.71-1.95 (2.02-1.95)	33.96-1.95 (2.02-1.95)	24.66-2.0 (2.07-2.0)
Merged lattices	25274	14980	15629	13596
Reflections observed (unique)[b]	16675375 (128780)	10382513 (128981)	9590816 (128969)	9549089 (116482)
Mean $\langle I\rangle/\sigma\langle I\rangle$ [a,b,c]	34.3 (0.8)	27.5 (0.6)	25.2 (0.6)	1.78 (0.32)
CC1/2 [a,b]	0.944 (0.282)	0.949 (0.175)	0.945 (0.077)	0.933 (0.25)
Completeness (%) [a,b]	99.93 (99.90)	99.91 (99.70)	99.84 (99.16)	99.06 (92.35)
R, R_{free}, test (%)[d]	16.24, 18.96, 1.55	17.54, 19.54, 1.55	16.77, 19.64, 1.55	20.36, 23.50, 1.71
R_{split} (%)	20.8 (100.6)	20.6 (110.8)	21.6 (119.8)	24.1 (90.8)
RMSD[e] bond length (Å)	0.017	0.004	0.010	0.007
RMSD[e] angles (deg)	1.33	0.72	0.99	0.81
Average B-factor	45.40	46.07	46.51	45.36
Ramachandran favored, allowed and outlier regions (%)	96.50, 3.33, 0.17	97.42, 2.58, 0.00	97.09, 2.91, 0.00	97.17, 2.83, 0.00

[a] Values for the highest resolution shell are given in parentheses. [b]These statistics are for merging the data in $P4_1$. The data were subsequently merged into $P4_12_12$, essentially halving the number of unique reflections and improving the completeness, $\langle I\rangle/\sigma\langle I\rangle$, and CC1/2 beyond what is reported here. [c]Columns 1-3: σ was computed using the Ha14 error model as described in Hattne, et al.[1] and Brewster et al. 2018.[2] Column 4: σ was computed using the Ev11 error model (see Brewster et al. 2018[2] and 2019[3]). The difference in error models accounts for the large difference in $\langle I\rangle/\sigma\langle I\rangle$ values when comparing columns 1-3 with column 4; see Brewster et al.[3] for more information. [d] $R = (\sum|F_{obs} - kF_{calc}|)/\sum|F_{obs}|$, where k is a scale factor. The R_{free} value was calculated with the indicated percentage of reflections not used in the refinement. [e] Root-mean-square deviation (RMSD) from ideal geometry in the final models.

Table S2. List of MMOH (α-Subunit) Residues that Undergo a Large Structural Rearrangement upon MMOB Binding.[a]

Position	Residues reorganized	Specific interaction with MMOB
Loop 2	A53, N54, E55, T56, K57, E58, Q59, F60, K61, V62	K57 hydrogen bond to D137 Q59 hydrogen bond to A115(b) K61 hydrogen bond to T136(b)
Helix A	R69	R69 hydrogen bond to D103
Helix A	R77	R77 hydrogen bond to E47
Helix B	L110	L110 steric clash with L216 (MMOH)
Helix E	L204, Q205, L206, V207, G208, E209, A210, C211, F212, T213, N214, P215, L216, I217, V218, A219, V220, T221, E222, W223	N214 hydrogen-bond to S110 V218 steric clash with F75
Helix F	F236, L237, S238, V239, E240, T241, D242, E243, L244, R245, H246, M247, A248, N249, G250, Y251, Q252	L237 hydrogen bond to S109(b) E240 steric clash with S109 L244 steric clash with T111 Y251 steric clash with L128
Loop 9	S256, I257, A258, N259, D260, P261, A262, S263	
Helix G	W276, F282, T283, L286, F290	
Loop 10	V298, E299	E299 hydrogen bond to Y8
Helix H, Loop 11 and Helix 4	V302, K303, T304, W305, N306, R307, W308, V309, Y310, E311, D312, W313, G314, G315, I316, W317, I318, G319, R320, L321, G322, K323, Y324, G325, V326, E327, S328, P329, A330, S331, L332, R333, D334, A335, K336, R337, D338, A339, Y340, W341, A342, H343	V302 steric clash with F20 K303 steric clash with N9 and M13 K303 hydrogen bond to L15(b) N306 steric clash with F24 R307 steric clash with Y8 W308 steric clash with P215 (MMOH) Y310 hydrogen bond to V31(b) D312 hydrogen bond to K79 I316 steric clash with S35 R320 steric clash with R114 R320 hydrogen bond to S126(b) K323 steric clash with L132 Y324 steric clash with L131 Y324 hydrogen bond to D132 R333 steric clash with Q30 R333 hydrogen bond with E27 K336 hydrogen bond to F24(b) and N29(b)

[a] The 1MHY and the 6YD0 structure have been compared in order to generate this table. The specific interactions between MMOH and MMOB residues are listed in the right-most column. Some MMOH residues interact with the main-chain atoms in MMOB and these have been indicated with the (b) symbol. Some MMOH residues reorganize as an indirect effect of MMOB binding for they interact with MMOH residues that rearrange as a result of direct interaction with MMOB.

Table S3. List of Hydrogen Bond Donor-Acceptor Distances (in Angstroms) in MMOH Alone (1MHY) and the Diferric (6YD0) and Diferrous Forms (6YDI) of the MMOH:MMOB Complex.

Donor Acceptor pair	1MHY	6YD0	6YDI
D242-H147	2.67	2.60	2.66
D242-R146	2.92	2.86	2.81
D242-E71	2.80	2.60	2.66
D242-K74	2.78	2.71	2.69
D143-H246	2.76	2.75	2.83
D143-R245	2.95	2.76	2.81
D143-Y67	2.68	2.62	2.61

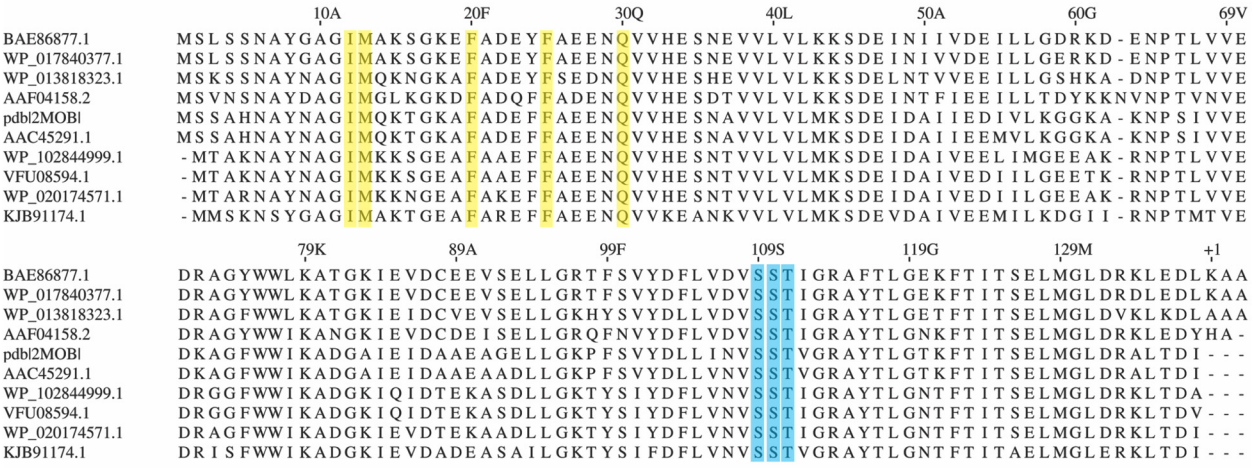

Figure S1. Multiple sequence alignment of the regulatory MMOB protein in sMMO enzymes. The strictly conserved residues on the N-terminal MMOB tail that interact with Helices H and 4 of MMOH are highlighted in yellow. The strictly conserved residues in the core of MMOB that interact with MMOH Helices E and F are highlighted in cyan. Sequences compared include - BAE86877.1 - *Methylomicrobium japanense*; WP_017840377.1 *Methylomicrobium buryatense*; WP_013818323.1 *Methylomonas methanica*; AAF04158.2 *Methylococcus capsulatus* Bath; pdb|2MOB| *Methylosinus trichosporium* OB3b; AAC45291.1 *Methylocystis sp.* M; WP_102844999.1 *Methylocella silvestris*; VFU08594.1 *Methylocella tundra*; WP_020174571.1 *Methyloferula stellate*; KJB91174.1 *Skermanella aerolata* KACC 11604.

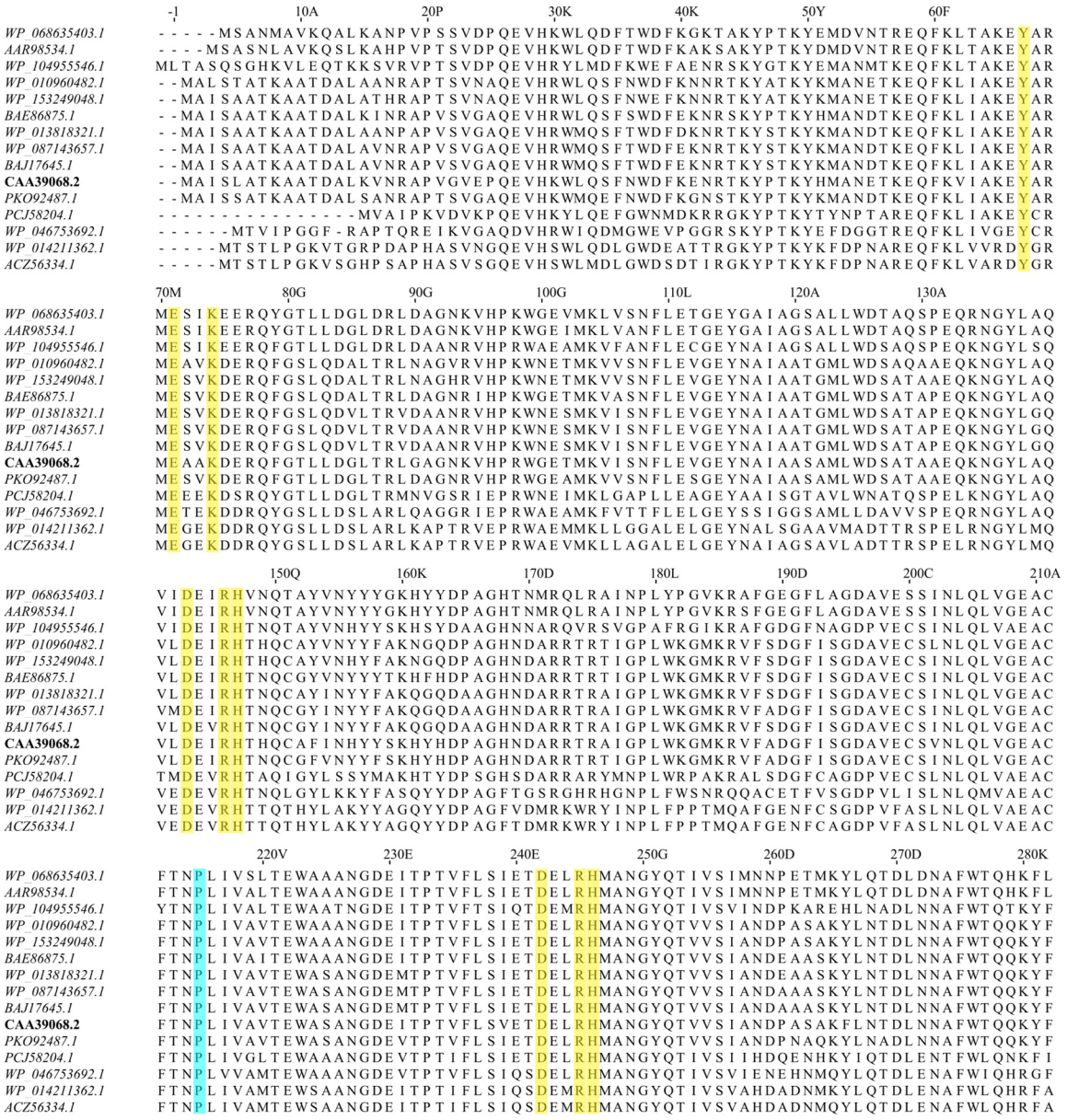

Figure S2. Multiple sequence alignment of a portion of the α-subunit of sMMOH in sMMO enzymes. The strictly conserved residues of the hydrogen bonding network distal to the histidine ligands are highlighted in yellow. The strictly conserved Pro215 residue in Helix E is highlighted in cyan. Sequences compared include the α-subunit of hydroxylase proteins for a butane monooxygenase - AAR98534.1 *Brachymonas petroleovorans*. The remaining sequences are for the α-subunit of hydroxylase proteins for methane monooxygenases - WP_068635403.1 *Thauera butanivorans*; WP_104955546.1 *Sphingobium sp*. SCG-1; WP_010960482.1 *Methylococcus capsulatus* Bath; WP_153249048.1 *Candidatus Methylospira mobilis*; BAE86875.1 *Methylomicrobium japanense*; WP_013818321.1 *Methylomonas methanica*; WP_087143657.1 *Crenothrix polyspora*; BAJ17645.1 *Methylovulum miyakonense* HT12; PKO92487.1 *Betaproteobacteria bacterium* HGW-Betaproteobacteria-1; PCJ58204.1 *Rhodospirillaceae bacterium*; WP_046753692.1 *Mycolicibacterium elephantis*; WP_014211362.1 *Mycolicibacterium rhodesiae*; ACZ56334.1 *Mycolicibacterium chubuense* NBB4.

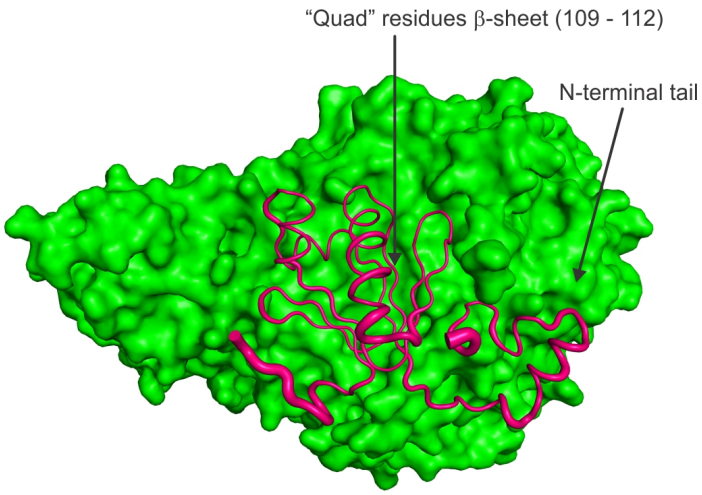

Figure S3. The B-factors of the MMOB protein in the diferric sMMOH:MMOB structure are represented as a putty cartoon figure in magenta. The MMOH surface is represented in green. Thicker secondary structure elements indicate high B-factor while thin regions indicate low B-factors.

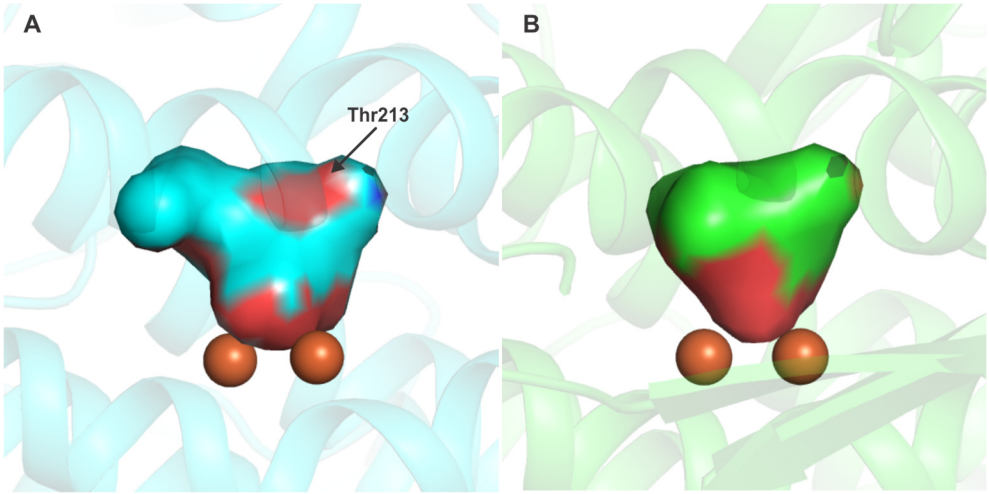

Figure S4. Surface representation of the sMMOH active site cavity depicts the difference in polarity in diferric MMOH (panel A) and the diferric MMOH:MMOB complex (panel B) as a result of the reorganization of Thr213.The side-chain of residues that project into the active site cavity are colored according to the following scheme; carbon atoms = cyan in MMOH, green in MMOH:MMOB; oxygen atoms = red; nitrogen atoms = blue. The iron atoms are shown as orange spheres.

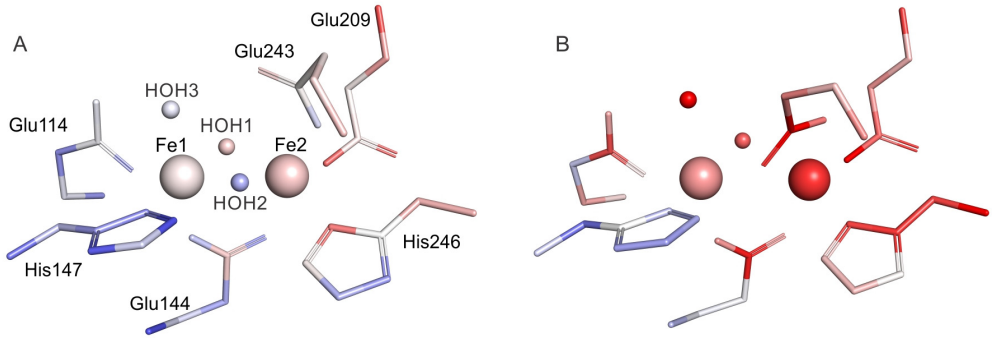

Figure S5. The diiron clusters of the diferric sMMOH:MMOB complex (6YD0, panel A) and diferrous sMMOH:MMOB complex (6YDI, panel B) are colored according to the atomic B-factors. A color spectrum from red to white to blue represent the B-factors, where red = 45, white = 35 and blue = 25.

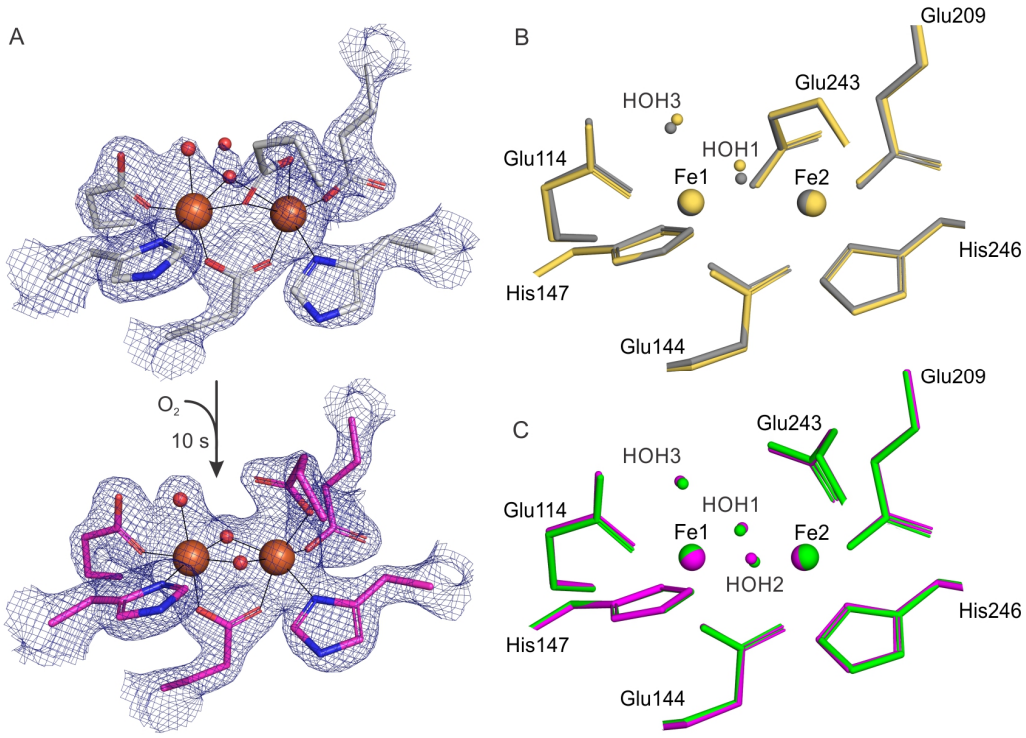

Figure S6. Diferrous sMMOH:MMOB crystals washed of reductant undergo reoxidation upon exposure to O_2 in the reaction region of the DOT (drop on tape) system while staying reduced if exposed to helium under identical conditions. Panel A: 2Fo-Fc map of the diiron cluster of sMMOH^{red}:MMOB immediately prior to O_2 exposure (6YY3, top) and after post-4s O_2 exposure, 6 s aging (6YDU, bottom) contoured to 2 σ. Panel B: An alignment of the diiron cluster of 6YY3 (grey atoms) with that of the diferrous sMMOH:MMOB complex (6YDI; yellow atoms) indicates that the sMMOH:MMOB crystals stay reduced in the absence of O_2 after removal of the dithionite reductant. Panel C: An alignment of 6YDU (purple atoms) with that of the diferric sMMOH:MMOB complex (6YD0; green atoms) indicates that the reduced sMMOH:MMOB crystals oxidize completely to the resting diferric state in this timeframe.

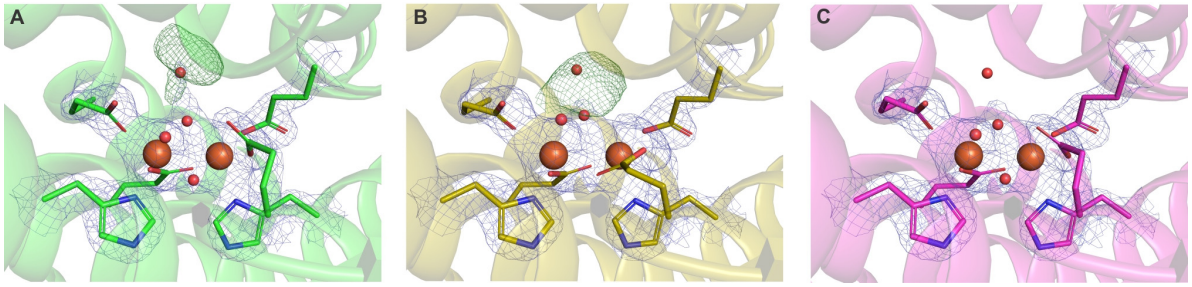

Figure S7. Loss of unassigned electron density (Fo-Fc electron density map (green mesh) contoured at 3σ, 2Fo-Fc electron density map (blue mesh) contoured at 2σ) from the active site post *in-crystallo* single turnover. Panel A: Diferric MMOH:MMOB complex (6YD0), Panel B: Reduced MMOH:MMOB complex (6YDI) and Panel C: Re-oxidized MMOH:MMOB complex (6YDU).

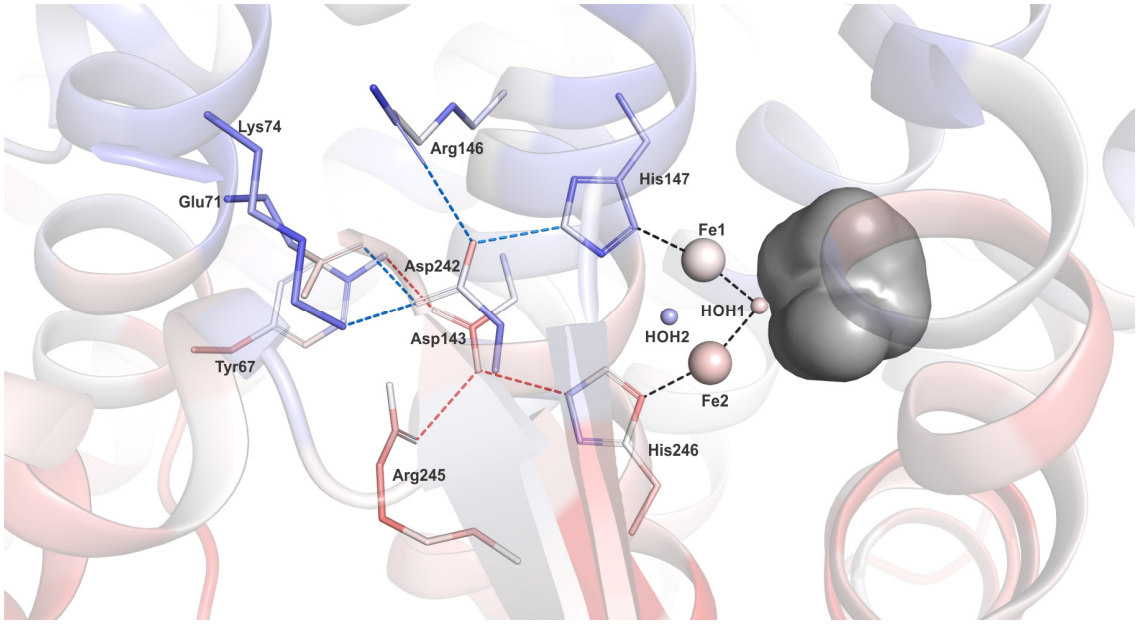

Figure S8. Top-down perspective of the hydrogen-bonding network on the distal side of the diiron cluster. The residues are colored according to its B-factor where blue indicates the lowest B-factor (25), red the highest (45) and white an intermediate value (35). The iron atoms are represented as larger spheres while the bridging μ-hydroxo groups are shown as smaller spheres. The active site cavity is shown as a grey surface. Black dashed lines depict the trans-positioning of the histidine ligands with respect to the μ-hydroxo moiety facing the active site. Red and blue dashed lines show the hydrogen bond network.

SUPPLEMENTAL REFERENCES

1. Hattne, J.; Echols, N.; Tran, R.; Kern, J.; Gildea, R. J.; Brewster, A. S.; Alonso-Mori, R.; Glöckner, C.; Hellmich, J.; Laksmono, H.; Sierra, R. G.; Lassalle-Kaiser, B.; Lampe, A.; Han, G.; Gul, S.; DiFiore, D.; Milathianaki, D.; Fry, A. R.; Miahnahri, A.; White, W. E.; Schafer, D. W.; Seibert, M. M.; Koglin, J. E.; Sokaras, D.; Weng, T.-C.; Sellberg, J.; Latimer, M. J.; Glatzel, P.; Zwart, P. H.; Grosse-Kunstleve, R. W.; Bogan, M. J.; Messerschmidt, M.; Williams, G. J.; Boutet, S.; Messinger, J.; Zouni, A.; Yano, J.; Bergmann, U.; Yachandra, V. K.; Adams, P. D.; Sauter, N. K., Accurate macromolecular structures using minimal measurements from X-ray free-electron lasers. *Nat. Methods* **2014,** *11*, 545-548.

2. Brewster, A. S.; Waterman, D. G.; Parkhurst, J. M.; Gildea, R. J.; Young, I. D.; O'Riordan, L. J.; Yano, J.; Winter, G.; Evans, G.; Sauter, N. K., Improving signal strength in serial crystallography with DIALS geometry refinement. *Acta Crystallogr., Sect. D: Struct. Biol.* **2018,** *74*, 877-894.

3. Brewster, A. S.; Bhowmick, A.; Bolotovsky, R.; Mendez, D.; Zwart, P. H.; Sauter, N. K., SAD phasing of XFEL data depends critically on the error model. *Acta Crystallogr., Sect. D: Struct. Biol.* **2019,** *75*, 959-968.